ACS Sustainable Chemistry & Engineering

pubs.acs.org/journal/ascecg

Research Article

Mesoporous Carbon Microfibers for Electroactive Materials Derived from Lignocellulose Nanofibrils

Ling Wang, Maryam Borghei,* Amal Ishfaq, Panu Lahtinen, Mariko Ago, Anastassios C. Papageorgiou, Meri J. Lundahl, Leena -Sisko Johansson, Tanja Kallio, and Orlando J. Rojas*

Cite This: ACS Sustainable Chem. Eng. 2020, 8, 8549–8561

Read Online

ACCESS | Metrics & More | Article Recommendations | Supporting Information

ABSTRACT: The growing adoption of biobased materials for electronic, energy conversion, and storage devices has relied on high-grade or refined cellulosic compositions. Herein, lignocellulose nanofibrils (LCNF), obtained from simple mechanical fibrillation of wood, are proposed as a source of continuous carbon microfibers obtained by wet spinning followed by single-step carbonization at 900 °C. The high lignin content of LCNF (~28% based on dry mass), similar to that of the original wood, allowed the synthesis of carbon microfibers with a high carbon yield (29%) and electrical conductivity (66 S cm^{-1}). The incorporation of anionic cellulose nanofibrils (TOCNF) enhanced the spinnability and the porous morphology of the carbon microfibers, making them suitable platforms for electrochemical double layer capacitance (EDLC). The increased loading of LCNF in the spinning dope resulted in carbon microfibers of enhanced carbon yield and conductivity. Meanwhile, TOCNF influenced the pore evolution and specific surface area after carbonization, which significantly improved the electrochemical double layer capacitance. When the carbon microfibers were directly applied as fiber-shaped supercapacitors (25 F cm^{-3}), they displayed a remarkably long-term electrochemical stability (>93% of the initial capacitance after 10 000 cycles). Solid-state symmetric fiber supercapacitors were assembled using a PVA/H_2SO_4 gel electrolyte and resulted in an energy and power density of 0.25 mW h cm^{-3} and 65.1 mW cm^{-3}, respectively. Overall, the results indicate a green and facile route to convert wood into carbon microfibers suitable for integration in wearables and energy storage devices and for potential applications in the field of bioelectronics.

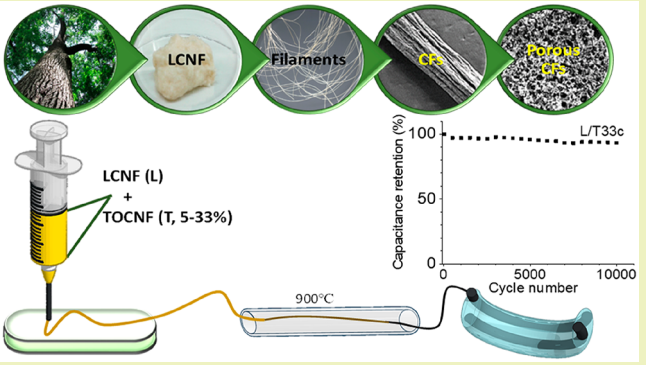

KEYWORDS: *Wood, Lignin, Nanocellulose, Wet spinning, Carbon fibers, Supercapacitance*

INTRODUCTION

Renewable resources are attractive alternatives for the growing demand of carbon fibers (CFs).[1] They include cellulose, which was reported already as early as the 1880s,[2] from cotton, ramie, and other natural fibers; however, the actual performance of the cellulose-based CFs is limited by several factors.[2,3] Carbon fibers made from regenerated cellulose after solvent spinning, such as Viscose, Lyocell, and Ioncell-F, show competitive properties given their high degree of polymerization, crystallinity, and polymer orientation along the fiber axis.[4] A drawback of related processes is the demand for pure cellulose to facilitate its dissolution in the solvent, for example, carbon disulfide, N-methymorpholine-N-oxide, ionic liquids, and sodium hydroxide solutions. These solvents may have negative impacts on the cost, equipment corrosion, and sustainability metric. Moreover, solvent recovery is required for these processes to be economically viable. Recent studies indicated cellulose nanofibrils (CNF) as possible precursors that require no dissolution for wet spinning, representing a simple, low cost, and eco-friendly technique.[5−8] In this process, aqueous suspensions of CNF are extruded into a coagulation bath comprising either an organic solvent (ethanol, acetone) or aqueous solutions (electrolyte or acidic solutions).[9] The formed filaments present high crystallinity and promising mechanical properties.[10] Unfortunately, the carbonization yield of such cellulose-based filaments is less than 20%, a consequence of the relatively low theoretical carbon content of cellulose, *ca.* 44%,[2] and the cleavage of glycoside linkages, bond scission, and loss of oxygen and hydrogen during carbonization.[11,12]

An alternative to cellulose is another plant-based polymer, lignin, with the advantage of a high carbon content (>60%); unfortunately, lignin is not easily spun into fibers. Lignin

Received: January 30, 2020
Revised: April 5, 2020
Published: May 13, 2020

https://dx.doi.org/10.1021/acssuschemeng.0c00764
ACS Sustainable Chem. Eng. 2020, 8, 8549−8561

modification or the addition of a secondary polymer plasticizer is generally required in the spinning process.[13] An additional drawback is the long thermal stabilization required to prevent fiber fusion during carbonization.[12,14,15] It was previously shown that the addition of nanocellulose to lignin prevents fiber fusion during carbonization, thus eliminating the need for tedious thermal stabilization; in turn, lignin increases the carbon yield and produces carbon fibers with good electrical conductivity.[16]

On the basis of the results reported so far, it is reasonable to consider another precursor, namely, lignocellulosic (nano)-fibrils, such as those derived from mechanical fibers, obtained without any chemical treatment (such as digestion and bleaching). Indeed, lignocellulose nanofibrils (LCNF) can be prepared from unbleached mechanical wood pulp via homogenization, microfluidization, and microgrinding.[17−19] The use of lignocellulose implies a better integration, lower costs, and more complete utilization of biomass and eliminates the need for polymer fractionation. It is surprising that such feedstock has not been explored as a precursor for CF, especially because mechanical defibrillation of wood has been known as an effective process to liberate fibers since the 18th century.[20] Limited dissolution of cell wall components in mechanical defibrillation results in fibrils with a high total mass yield (97−98%) compared to the typical chemical routes (45−50%).[21] Several products are obtained from mechanical fibers, such as unbleached printing paper, board grades, wallpaper, and absorbent and molded products.[22] Recently, Nguyen et al. successfully spun fibers from autohydrolyzed wood chips via ionic liquid dissolution.[23]

Here, mechanical wood fibers were used to produce lignocellulose nanofibrils (LCNF), which were further processed via wet spinning. Taking advantage of the presence of cellulose and lignin, they were directly carbonized into carbon microfibers, thereby eliminating the need for thermal stabilization. Unfortunately, LCNF alone did not form filaments or microfibers by wet spinning. Therefore, an aid was necessary and, in the present case, a small loading of lignin-free nanofibers, such as TOCNF, improved LCNF spinnability (for example, a TOCNF concentration as low as 5% was sufficient to allow spinnability). Other possible components can be considered, but TOCNF was taken as a good reference given that several recent studies have made extensive use of this type of nanocellulose. Increased levels of TOCNF loading (up to 33%) significantly influenced the properties of the spun fibers, before and after carbonization. TOCNF contributes to pore evolution during carbonization, saving steps such as surface activation; electrochemical treatment;[24] and deposition of particles (CNTs/GO),[25] conductive polymers, or metal-oxides,[26−28] which are otherwise required for energy storage application. The reported resources and methods pave the way toward cost-effective fiber-shaped supercapacitors that are proposed for integration into small portable devices and woven wearable electronics.[29−33]

EXPERIMENTAL SECTION

Materials. Never-dried unbleached mechanical softwood pulp and bleached birch fibers were kindly provided by Sappi's Kirkniemi Mill and UPM's Pietarsaari Mill, both in Finland. Acetone, 2,2,6,6-tetramethylpiperidine-1-oxyl (TEMPO), poly(vinyl alcohol) (PVA), poly(dimethylsiloxane) (PDMS), and sodium hydroxide were purchased from Sigma-Aldrich and used without further purification.

Lignocellulose (LCNF) and TEMPO-Oxidized Cellulose (TOCNF) Nanofibrils. Never-dried unbleached mechanical pulp with a dry solids content of 1.8 wt % was first subjected to pregrinding (two passes) with a super mass colloider (MKZA10−15J, Masuko Co. Ltd., Japan) operating at 1500 rpm with a gap of 0.22 mm and 0.18 mm. Then, the fibrils were further refined through one and five passes in high-pressure microfluidization (Microfluidizer M-110EH-30) operating at 1100 and 1800 bar, respectively. The resultant LCNF was concentrated to 6.1 wt % after centrifugation at 2000 rpm for 10 min.

TOCNF was prepared according to the literature.[16] Briefly, never-dried bleached hardwood (birch) pulp was oxidized by TEMPO at pH 10, then washed with deionized water. The TEMPO-oxidized fibrils were refined through one-pass high-pressure microfluidization (Microfluidics Corp., USA). The TOCNF obtained had 1.6 wt % solid content and 0.6 mmol g^{-1} carboxylic groups. In this paper, TOCNF was used as a reference and to enhance the spinnability of LCNF.

Nanofibril Composition and Morphology. To determine the carbohydrate and lignin content in LCNF, the same composition as that of the precursor mechanical pulp was assumed, which was dried in an oven at 80 °C and Wiley-milled through a 60-mesh sieve after cooling down. Sulfuric acid was used in a two-step procedure run in duplicate according to NREL/TP-510-42618.[34] To investigate the fibrils' morphology, TOCNF and LCNF suspensions were diluted and cast on a mica support by spin coating and then dried at 50 °C for 1 h. The dried samples were imaged with an AFM (Nanoscope V controller, Bruker Corporation, USA) using an E-scanner in the air and operating in tapping mode.

Wet Spinning of LCNF/TOCNF Dope and Carbonization. Aqueous suspensions of TOCNF of a given composition (0, 5, 13, 20, 33, and 100% TOCNF, based on total dry mass) was added to 50 g of 6.1% LCNF. The mixed dopes were stirred (3 min at 2000 rpm) and degassed (3 min at 2500 rpm) via a planetary centrifugal mixer (THINKY ARE-250). The prepared suspensions or dopes were loaded into a 50 mL plastic syringe connected with a plastic tube (44.5 cm in length and 6 mm in inner diameter) that ended in a needle with an inner diameter of 1.2 mm and a length of 3.7 cm. The latter was immersed in a coagulation bath (acetone) during spinning at a fixed rate of 10 mL min^{-1}. After approximately 1 min, filaments were collected from the acetone antisolvent and dried under tension under room temperature (23 °C) conditions. The wet-spun microfibers contained the given TOCNF amount, therein referred to as LCNF, L/T5, L/T13, L/T20, L/T33, and TOCNF, respectively. The wet-spun microfibers were carbonized in a tubular furnace (NBD-O1200−50IC Vacuum Tube, Furnace) at 900 °C for 60 min operated at a heating rate of 2 °C min^{-1} under a N_2 flux. After carbonization, carbon microfibers were obtained and named following the same nomenclature as before but adding a subscript, the letter "c" standing for carbonization, namely, LCNFc, L/T5c, L/T13c, L/T20c, L/T33c, and TOCNFc. The carbonization yield was calculated from the mass before and after carbonization.

Bulk Density and Morphology. The bulk density of the wet-spun microfibers was obtained by weighing and measuring the volume of the microfibers, assumed to have a circular cross section. Seven specimens were measured for each sample. The surface and cross-section of the microfibers at the break point, before and after carbonization, were observed by field emission scanning electron microscopy using a Zeiss SIGMA VP (Carl Zeiss Microscopy Ltd., Cambridge, UK) at 1.6 kV. The working distance was 1 cm. Before imaging, the microfibers before carbonization were sputter-coated with a 5 nm thickness of Pt/Pd.

Wide Angle X-ray Scattering (WAXS) and Raman Spectroscopy. WAXS was used to determine the orientation of cellulose crystallites in TOCNF, which was assumed to indicate the orientation of nanofibrils in the wet-spun microfibers. A MicroMax-007 HF X-ray generator (Rigaku, Japan) was operated at a wavelength of 1.54 Å, with a beam size of 120 μm and exposure time of 10 min. A Mar345 imaging plate detector was used to collect sample diffraction patterns with a 200 mm sample-to-detector distance. Before evaluation,

https://dx.doi.org/10.1021/acssuschemeng.0c00764
ACS Sustainable Chem. Eng. 2020, 8, 8549−8561

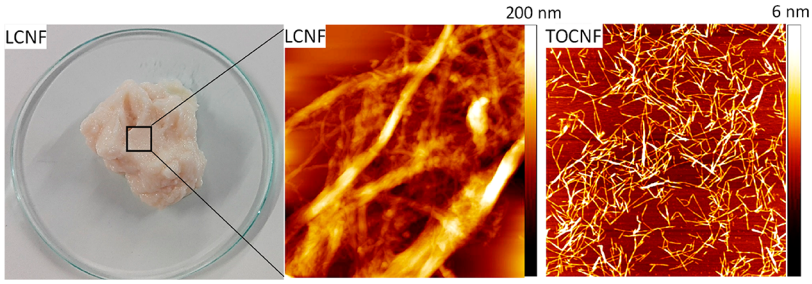

Figure 1. A photograph of LCNF hydrogel and AFM images (3 × 3 μm) of LCNF and TOCNF.

Table 1. Composition of the Spinning Dope, Dope Spinnability, and Properties of the Obtained Microfibers before Carbonization (L = LCNF, T = TOCNF)

	LCNF	L/T5	L/T13	L/T20	L/T33	TOCNF
spinnability	no	yes	yes	yes	yes	yes
density, g cm^{-3}	N/A	1.13 ± 0.20	1.17 ± 0.09	1.31 ± 0.24	1.34 ± 0.21	1.32 ± 0.13
Young modulus, GPa	N/A	2.8 ± 0.97	5.8 ± 1.43	6.7 ± 1.2	8.5 ± 2	15.2 ± 2.6
tensile strength, MPa	N/A	45 ± 17	106 ± 24	154 ± 60	150 ± 21	215 ± 65
strain at break,%	N/A	3.2 ± 1	5.5 ± 2	7.0 ± 1	5.1 ± 1	4.6 ± 1
tenacity, cN tex^{-1}	N/A	14.5 ± 2	15 ± 1	15 ± 2	15.7 ± 1	17.4 ± 2
orientation index	N/A	0.67	0.70	0.74	0.74	0.74
Herman's parameter	N/A	0.57	0.61	0.66	0.66	0.64
T_{onset}, °C	281	277	270	265	255	230

diffraction patterns were corrected by subtracting the background. On the basis of azimuthal intensity distribution profiles, the orientation index (π) and Herman's orientation parameter (S) were calculated according to eqs 1 and 2.[35]

$$\pi = \frac{180^\circ - \mathrm{FWHM}}{180^\circ} \tag{1}$$

$$S = \frac{3\langle\cos^2\gamma\rangle - 1}{2} \tag{2}$$

where fwhm is the full width at the half-maximum (in degrees) of a peak in the azimuthal intensity distribution profile. The average $\langle\cos^2\gamma\rangle$ is obtained from the average cosine of the azimuthal angle φ based on eqs 3 and 4.

$$\langle\cos^2\gamma\rangle = 1 - 2\langle\cos^2\varphi\rangle \tag{3}$$

where

$$\langle\cos^2\varphi\rangle = \frac{\sum_{\varphi_0}^{\varphi_0+\pi/2} I(\varphi)\sin\varphi\cos^2\varphi}{\sum_{\varphi_0}^{\varphi_0+\pi/2} I(\varphi)\sin\varphi} \tag{4}$$

where $I(\varphi)$ is the intensity detected at azimuthal angle φ and φ_0 is the azimuthal angle in the beginning of the range used for the calculation of the average cosine $\langle\cos^2\varphi\rangle$. S was calculated at a φ_0 of 0, $\pi/2$, π, and $3\pi/2$, and the average of these values is reported.

Raman analysis was performed using a Horiba LabRAM HR spectrometer equipped with a CCD camera and a 633 nm excitation laser.

Specific Surface Area and Mechanical Strength. The specific surface area of the carbon microfibers was characterized by N_2 adsorption/desorption using the Brunauer, Emmett, and Teller (BET) method. The nonlocal density functional theory (NLDFT) was used to analyze the pore volume.

The tensile strength of the wet-spun microfibers was measured by using an Instron 5944 Single Column, Tabletop Universal Testing System operated in tensile mode with a load cell of 5 N. Before testing, all the microfibers were conditioned overnight in 50% relative humidity at 23 °C. The diameter of the microfibers was measured by a micrometer assuming a circular cross section. Eight specimens of each sample were tested with an extension rate of 2 mm min^{-1} and a gauge length of 20 mm.

Thermogravimetric Analysis (TGA). TGA was utilized for the characterization of the microfibers' thermal stability by measuring the weight change as a function of temperature in N_2 atmosphere (TA Instrument, Thermo Gravimetric Analyzer Q500). The wet-spun microfibers were cut into small pieces and heated up to 900 °C from room temperature at a heating rate of 10 °C min^{-1}. As a reference, LCNF was also measured after drying in an oven at 80 °C and ground through a 60-mesh sieve.

Electrical Conductivity of Carbon Microfibers. Each given carbon microfiber was fixed on a support with silver paint, and the diameter was measured using a microscope and the length with a ruler. The electrical conductivity of the carbonized microfiber was calculated based on eq 5. The electrical resistance was determined with a semiconducting parameter analyzer (Agilent 4154A) operated under ambient conditions. These tests were run in duplicate and six times for each sample.

$$\sigma = \frac{l}{RA} \tag{5}$$

where σ is the conductivity of the material (S cm^{-1}), R is the resistance of the specimen (Ω), and l and A are, respectively, the length (cm) and cross-sectional area of the specimen (cm^2).

Electrochemical Capacitance and All-Solid State Fiber-Shaped Supercapacitor Assembly. The carbon microfibers were used as free-standing working electrodes, assembled into a three-electrode cell configuration with Ag/AgCl as a reference and a platinum rod as a counter electrode. An Autolab PGSTAT12 potentiostat (EcoChemie, Netherlands) was used for electrochemical evaluation controlled by GPE software. Cyclic voltammetry (CV) measurements were carried out at a potential window from 0 to 0.8 V in 1 M H_2SO_4 as an electrolyte. Galvanostatic charge/discharge tests were also performed using various current densities over the voltage range of 0 to 0.8 V. Electrochemical impedance spectroscopy (EIS) was carried out at open circuit voltage over a frequency range of 0.01 Hz to 100 kHz.

The supercapacitor assembly used two carbon microfibers that were placed parallel on polydimethylsiloxane (PDMS) films, and the overlapping section was coated with PVA/H_2SO_4 gel electrolyte at room temperature. After the electrolyte became a gel, the assembly

https://dx.doi.org/10.1021/acssuschemeng.0c00764
ACS Sustainable Chem. Eng. 2020, 8, 8549−8561

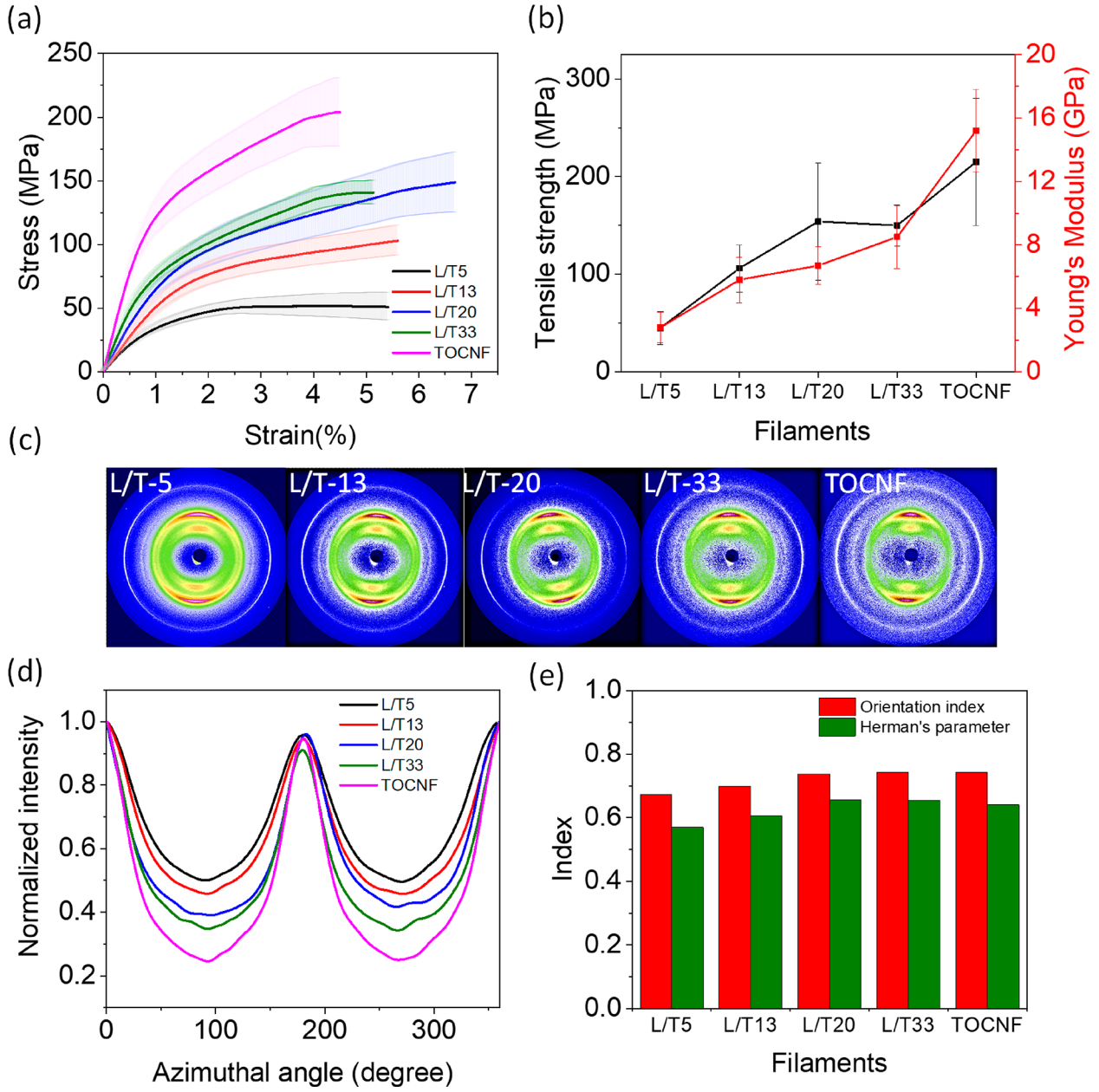

Figure 2. (a) Stress−strain profiles of LCNF-based microfibers (filaments) with given TOCNF content, from 5 to 100% (the standard derivations are highlighted around the curves). (b) Tensile strength and Young's modulus of microfibers as a function of TOCNF content. (c) 2D WAXS spectra of the LCNF/TOCNF microfibers. (d) Intensity in terms of azimuthal angle. (e) The orientation index and Herman's parameter of LCNF/TOCNF microfibers.

was covered with another layer of PDMS film to seal the whole system. Once the PDMS was dried at room temperature, the full fiber-shaped supercapacitor was ready to be used. The gel electrolyte was prepared by mixing 1 g of H_2SO_4 with 10 g of poly(vinyl alcohol) solution (PVA, 10%) at 90 °C.

RESULTS AND DISCUSSION

LCNF Composition and Fibril Morphology. Unbleached mechanical fibrils containing cellulose (36.5%), hemicellulose (29%), and lignin (28.3%; Table S1) were defibrillated into the nano/microsize (LCNF) to synthesize filaments by wet spinning (herein termed microfibers, given their size). The chemical composition of LCNF is expected to be quite similar to that of the crude raw fibrils.[22,36] The present work is motivated by the fact that a high lignin concentration facilitates high carbonization yield while hemicelluloses and cellulose introduce porosity features in the resultant carbon microfibers and remove the need for thermal stabilization.

Despite the high lignin content (28.3%), the LCNF aqueous suspension and hydrogels presented an off-white color (Figure 1), much lighter than the dark brown of the unbleached chemical fibers that contain chromophore groups formed from residual lignin.[37,38] For a given lignin content, mechanical fibers have a light-scattering coefficient that is higher than that of chemical fibers (50−65 m^2/kg compared to 30 m^2/kg), thus resulting in a brighter color.[39] TOCNF consists of homogeneous nanofibrils, whereas LCNF is heterogeneous in size, presenting nanofibril and microfibril bundles (Figure 1), as reported in other studies.[36,40]

https://dx.doi.org/10.1021/acssuschemeng.0c00764
ACS Sustainable Chem. Eng. 2020, 8, 8549−8561

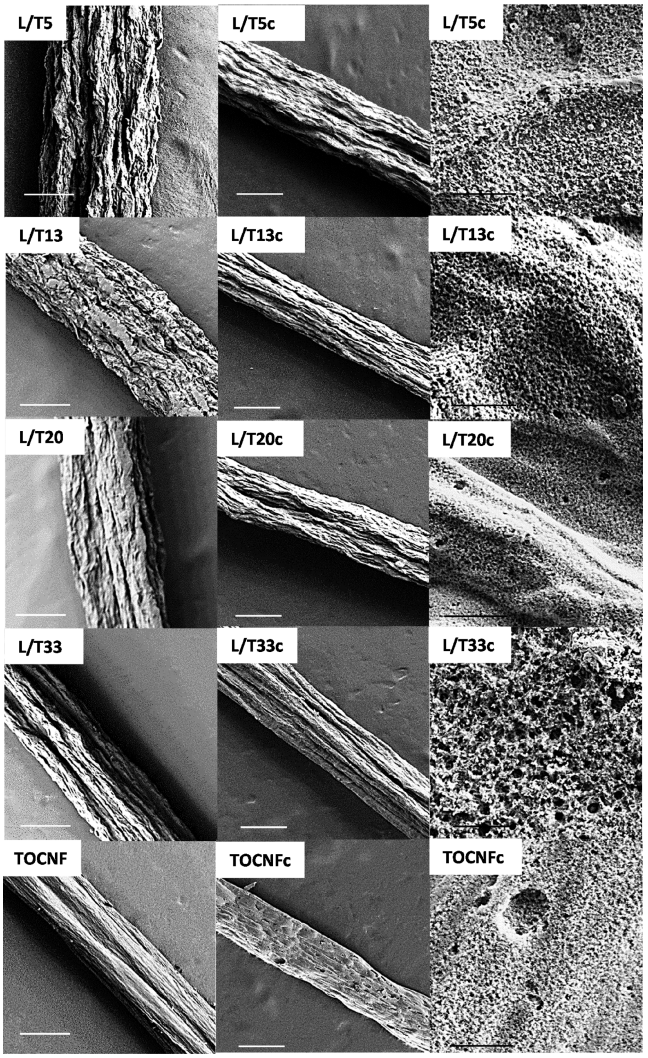

Figure 3. Surface morphology of the LCNF/TOCNF microfibers before (first column) and after (second column) carbonization (scale bar = 100 μm). Higher magnification images of the carbon microfibers are included in the third column (scale bar = 2 μm).

LCNF Wet-Spinning and Microfiber Density. Spinning dopes were prepared with different ratios of LCNF and TOCNF (0, 5, 13, 20, 33, and 100%) and spun into microfibers using acetone as an antisolvent for coagulation. LCNF alone (0% TOCNF) was not spinnable. However, the addition of small amounts of TOCNF (5%) significantly improved the LCNF spinnability. Further addition of TOCNF enhanced the spinning process. The lack of spinnability for LCNF is explained by the poor fibril bonding capacity,[22,36] an effect that is impaired by the thick bundles seen in LCNF (Figure 1). TOCNF, with a high fibril aspect ratio, enables better physical entanglement between fibrils during spinning.

Table 1 presents the density of the wet spun microfibers with various TOCNF content (5−33%). The values are in a close range (~1.1−1.3 g cm^{-3}). A slight difference was noticed at low TOCNF content, L/T5 and L/T13, which presented a lower density compared to microfibers L/T20, L/T33, and TOCNF. Because of the low bonding capacity of LCNF, a relatively loose structure could be formed in microfibers of high LCNF content.

Mechanical Strength and Orientation. The stress−strain curves and Young's modulus of the LCNF-based microfibers are displayed in Figure 2a and b, respectively. With increasing TOCNF content, from 5% to 33%, the Young's modulus and tensile strength of the microfibers increased, from 2.8 to 8.5 GPa and from 45 to 150 MPa, respectively (Table 1). The latter contained 67% of LCNF (L/T33) was 3 times stronger compared to microfibers with only 35% LCNF (48.6 ± 10 MP).[36] On the other hand, these values are still lower than those of microfibers produced from neat TOCNF (15 GPa Young modulus and 215 MPa tensile strength).

The orientation index and Herman's parameter (WAXS) were used as an indicator of the orientation of cellulose crystallites in the lateral direction, with 0 and 1 corresponding to fully disordered and fully aligned fibrils, respectively. The 2D detector images in Figure 2c indicate crystals more aligned in the microfibers when the (200) diffraction rings are reduced to arcs. Clearly, as the TOCNF content is increased, the arcs become better defined or sharper, indicating a higher fibril orientation. This is further confirmed by the azimuthal intensity profiles (Figure 2d) where the peaks also become sharper. The nanocellulose orientation within the microfibers plays a significant role in defining the mechanical properties, especially the Young's modulus.[5,41−43] Accordingly, the higher TOCNF content in the dope, the better the fibril alignment, as indicated by both the orientation index and Herman's parameter: the orientation index increases from 0.67 to 0.74 and the Herman's parameter from 0.57 to 0.66, reaching a plateau for L/T20. The presence of amorphous lignin and branched hemicellulose in LCNF may impair fiber alignment during wet spinning. Meanwhile, the addition of TOCNF, from 5 to 33%, reduced the total solid content of the spinning dope (from 6.1% to 1.6%), providing more space for fibrils to move and align under shear.[43] The trend for the Herman's parameter does not correlate with the measured strength, i.e., the Young's modulus increases with TOCNF addition, as shown in Figure 2b. Noting that WAXS provides data originated from cellulose crystal alignment,[35] the presence of lignin and hemicelluloses impairs the interpretation of the orientation index as well as Herman's parameter. Therefore, they are taken here on a relative basis.

Table 2. Properties of the Carbonized Microfiber

microfiber	L/T5c	L/T13c	L/T20c	L/T33c
specific surface area, m^2 g^{-1}	12	20	17	46
pore volume, cm^3 g^{-1}	0.0033	0.0081	0.0094	0.0084
avg. pore size, nm	2.7	4.5	4.7	4.2
carbon yield, %	28.5 ± 1.6	28.9 ± 1.2	28.8 ± 0.9	22.2 ± 4.3
conductivity, S cm^{-1}	58.0 ± 6.2	62.3 ± 12.1	46.6 ± 8.2	42.5 ± 5.7
capacitance, F cm^{-3}	2.4 ± 1.4	5.3 ± 1.6	12 ± 3.3	25 ± 6.5

https://dx.doi.org/10.1021/acssuschemeng.0c00764
ACS Sustainable Chem. Eng. 2020, 8, 8549−8561

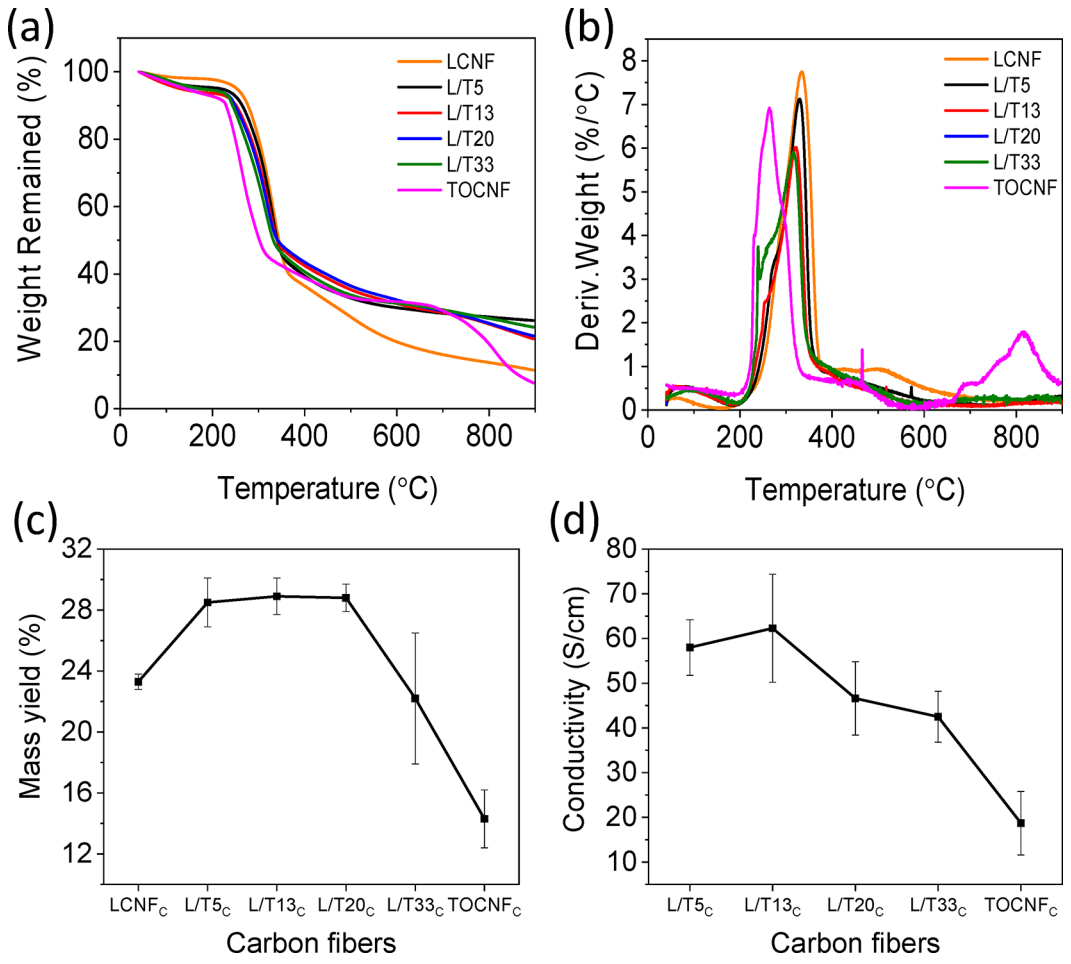

Figure 4. (a) TGA analysis and (b) DTG of LCNF/TOCNF microfibers, as indicated. (c) Carbonization yield and (d) respective electrical conductivity of LCNF/TOCNF microfibers.

Microfiber Morphology. Figure 3 shows the morphology of the LCNF/TOCNF microfibers, before and after carbonization. At higher TOCNF content, the microfibers become thinner and smoother on the surface. The cross-sectional images (Figure S1) further confirm that the addition of TOCNF results in smaller microfiber diameters. Upon carbonization, the microfibers shrink slightly along the transverse axis (Figure 3, second column). Compared to L/T13c, L/T20c, amd L/T33c keeping in straight form (Figure S2), TOCNFc and L/T5c become coiled upon carbonization.

The high magnification SEM images (Figure 3, third column) indicate a porous morphology for all carbon microfibers, with larger pores observed for the L/T33c. To gain more insights into the pore structure, nitrogen adsorption/desorption was carried out. The isotherms show higher adsorption as the TOCNF content was increased from 5 to 33% (Figure S3), leading to higher specific surface area, from 12 to 46 $m^2\ g^{-1}$ (Table 2). SEM images from cross sections of carbon microfibers illustrate a more porous structure for those with higher TOCNF content (Figure S4). Pore development with increased addition of TOCNF likely resulted from the cleavage of glycoside bonds and gasification. Li et al. also reported the effect of TOCNF in pore evolution in carbon microfibers obtained from graphene and TOCNF.[44] Overall, the specific surface area of our microfibers is in the range observed for natural hemp fibers (42.8 m^2g^{-1}).[45]

Carbonization and Properties of Carbon Microfibers. The thermal stability of the microfibers was investigated using TGA (Figure 4). TGA also provides information on how the various concentrations of TOCNF in the spinning dope affect the carbonization process and the left-over yield (carbon yield). Three stages for weight loss were observed for all the samples. The first transition (<200 °C) corresponds to the loss of water as well as elimination of small molecules.[46] Then, polymer decomposition and chain scission start (hemicellulose ~200−315 °C, cellulose ~315−400 °C, and lignin ~160−600 °C),[47] followed by carbonization until 900 °C.[48] The degradation and pyrolysis behavior of the microfibers were slightly different depending on their composition, Figure 4. Pure TOCNF microfibers started to decompose (T_{onset}) at 230 °C. The presence of sodium in TOCNF reduces the onset of decomposition temperature due to the catalytic dehydration and decarboxylation reactions, which facilitate char formation.[49,50] With a higher LCNF loading, e.g., with a higher lignin content, the T_{onset} increased to 277 °C for L/T33, close to the T_{onset} of LCNF microfibers (281 °C). The higher thermal resistance of the fibers containing more LCNF eventually improves the carbon yield, which affects the conductivity of the fibers after carbonization. Meanwhile, a clear trend was noticed from the thermogravimetry derivative (DTG). As shown in Figure 4b, the temperature at the maximum degradation rate was shifted to higher values (from 259 to 329 °C) with increased LCNF content.

https://dx.doi.org/10.1021/acssuschemeng.0c00764
ACS Sustainable Chem. Eng. 2020, 8, 8549−8561

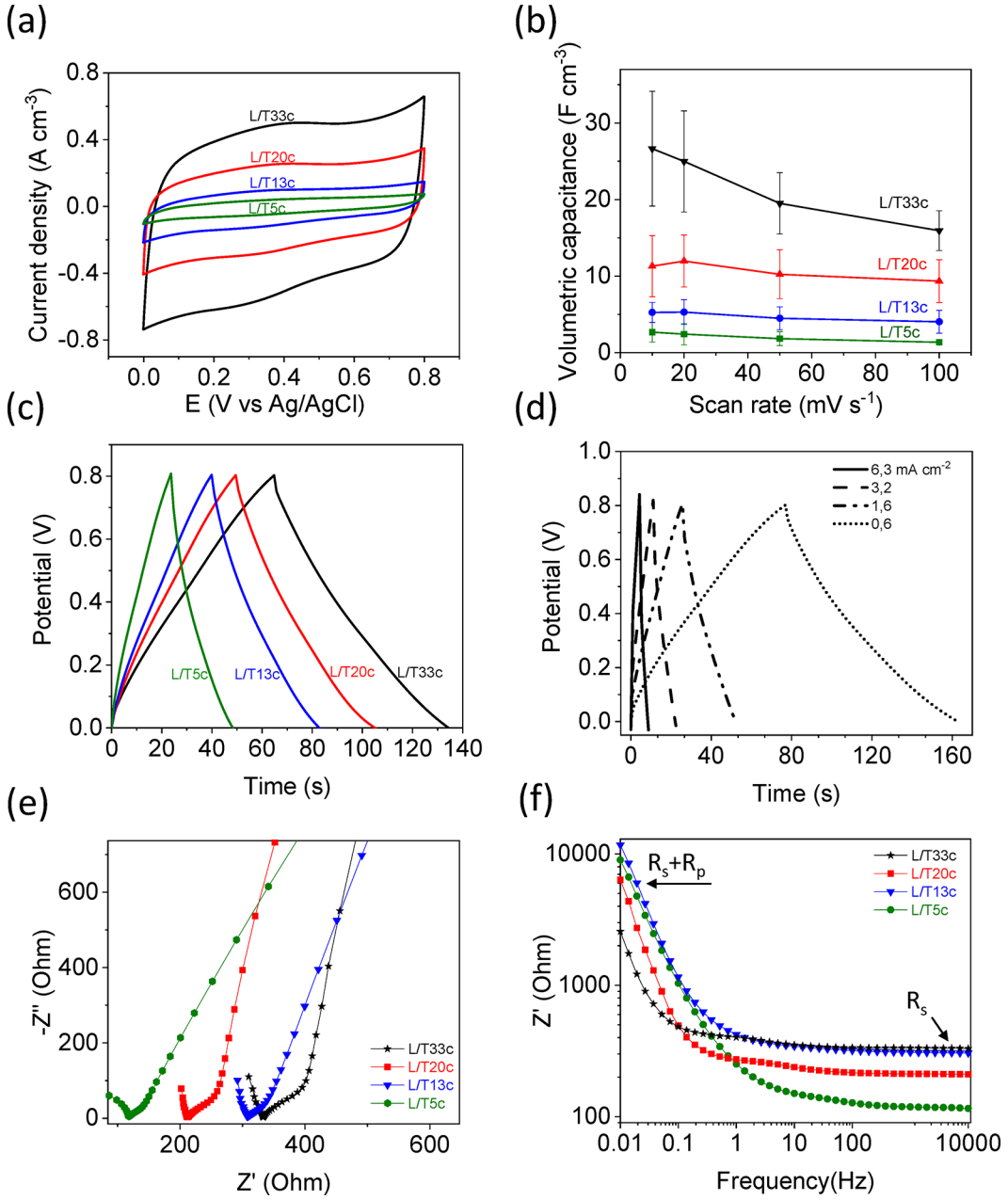

Figure 5. (a) CV curves of the carbonized LCNF/TOCNF fibers in 1 M H_2SO_4 at 20 mV s^{-1}. (b) Volumetric supercapacitance of carbon microfibers over various scan rates. (c) GCD of carbon microfibers at 0.6 mA cm^{-2}. (d) GCD of L/T33c at different current densities from 0.6 to 6.3 mA cm^{-2}. (e) Nyquist and (f) Bode plots recorded in the frequency range of 100 kHz to 0.01 Hz (the figure is shown to 10 kHz for better resolution). The standard deviations shown as error bars are the result of measurements carried out with four different series.

LCNF/TOCNF-based microfibers were carbonized in a tubular furnace at 900 °C for 60 min, and the respective mass yield was determined, Figure 4c. The carbonization yield of freeze-dried LCNF was 23%. Interestingly, the yield increased to 28.5% after transforming LCNF into microfibers by adding 5% TOCNF (L/T5c), and a plateau was kept until L/T20c. Then, it was dropped to 22% for L/T33c, which is still much higher than the carbonization yield of neat TOCNF microfibers (~14%). It is apparent that the microfiber composition has a significant influence on the carbonization yield. In addition, the electrical conductivity of the microfibers was influenced by the precursor composition (Figure 4d). TOCNFc showed the lowest electrical conductivity (~18 S cm^{-1}). The increase of LCNF concentration in the precursor dope clearly improved the microfiber conductivity, reaching to values 5-fold higher, ~62 S cm^{-1} for L/T13c, similar to that of L/T5c. Interestingly, the conductivity of our microfibers is close to the one reported in the literature for wet-spun graphene/cellulose nanocrystals (~65 S cm^{-1}).[51] Park et al. reported a 6-fold increase in electrical conductivity of wet-spun graphene fibers, from 23 to 133 S cm^{-1}, when CNTs were added to the spinning dope as intercalating material.[52] We have previously reported that the addition of 60% lignin to TOCNF dope significantly improved the electrical conductivity of the carbonized fiber, from ~40 to 103 S cm^{-1}.[16] Therefore, even though the fibril alignment and packing density are enhanced by TOCNF, the electrical conductivity

https://dx.doi.org/10.1021/acssuschemeng.0c00764
ACS Sustainable Chem. Eng. 2020, 8, 8549−8561

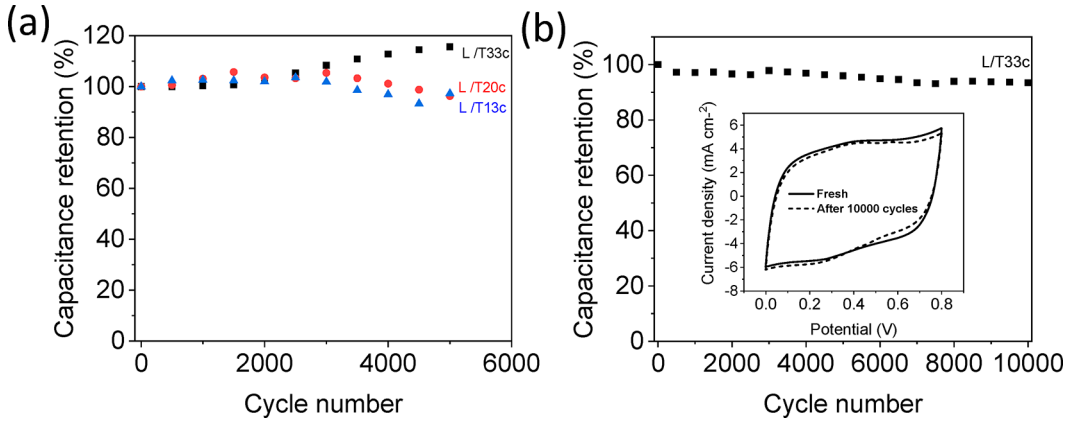

Figure 6. (a) Capacitance retention of carbon microfibers during 5000-cycle stability tests at 20 mV s^{-1} in 1 M H_2SO_4. (b) Stability evaluation of L/T33c during 10,000 cycles at 100 mV s^{-1} in 1 M H_2SO_4 (inset: CV of L/T33c before and after 10,000 cycles at 50 mV s^{-1}).

after carbonization is mainly influenced by residual lignin in the spinning precursor, given its higher carbon content.

Raman spectra of the carbon microfibers indicate the degree of graphitization (Figure S5). The G band located around 1600 cm^{-1} is related to the tangential vibration of the hybridized sp^2 carbon atoms in graphitic planes. The band around 1350 cm^{-1} is the characteristic breathing vibration mode, related to defects in the aromatic rings. The intensity ratio of the D to G bands (I_D/I_G) correlates with ratio of the disordered carbon structure to the graphitic planes. The I_D/I_G ratio for all the samples was similar (1.2 ± 0.1), since they were all carbonized at the same temperature (900 °C) and reached a similar graphitic carbon structure.[53]

Electrochemical Performance. Supercapacitors store energy either by electrochemical double layer capacitance (EDLC), via reversible ion adsorption/desorption or by pseudocapacitance (PC), via surface redox reactions. Owing to their high conductivity and porous morphology, the LCNF/TOCNF-derived carbon microfibers are suitable for EDLC. EDLC operates through electrostatic accumulation of charged ions and polar solvents at the electrode/electrolyte interface. Thus, the porous morphology of the electrode is advantageous, and the capacitance is proportional to the amount of stored charge. While PC results from Faradaic redox reactions at the surface of an electrode, it requires additional materials with different oxidation states such as metal oxides or conductive polymers. Thus, more complicated core−shell structures may be required for PC.[54−58]

The electrochemical behavior of the carbon microfibers was investigated in a three-electrode cell, and cyclic voltammetry (CV) was recorded from 0 to 0.8 V (vs Ag/AgCl) in 1 M H_2SO_4 at various scan rates (from 5 to 100 mV s^{-1}). The CV curves of all carbon microfibers showed symmetrical and rectangular shapes, even at higher scan rates, indicating typical features of EDLC and fast charge/discharge behavior (Figure S6). The slight pair of redox peaks was observed at −0.4 V due to the typical transition between quinone/hydroquinone groups commonly detected on carbon materials in sulfuric acid electrolyte.[59] Figure 5a compares the CV curves of the carbon microfibers derived from the different precursors measured at a scan rate of 10 mV s^{-1}. The increased TOCNF loading (from 5 to 33%) significantly improved the total area in the CV profiles, which indicates an increased specific surface area and porosity, as observed in Table 2 and Figure 3S. The specific capacitance obtained from CV profiles at 10 mV s^{-1} indicates the highest value for L/T33c (~25 F cm^{-3}) followed by L/T20c (~12 F cm^{-3}), L/T13c (~5.3 F cm^{-3}), and finally L/T5c (~2.4 F cm^{-3}; Figure 5b). Thus, a correlation exists between TOCNF loading in the precursor system and the capacitance behavior, highlighting the role of TOCNF in creating pores during carbonization. We note that for the L/T20c sample, a lower average capacitance at 10 mV/s is measured compared to that at 20 mV/s. While the differences are within the experimental error, any effect would likely be a consequence of the pore structure of the respective carbon microfiber.

As shown in the adsorption isotherms (Figure S3), there is a large difference in values recorded for the adsorption isotherm of L/T33c and the rest of systems. In addition, there is a more noticeable hysteresis loop for L/T33c, from relative pressure $P/P_0 = 0.4$ to 0.9, revealing the coexistence of both micropores and mesopores, both of which contribute to the EDLC. In particular, mesopores are main contributors in the diffusion of ions to the micropores. Considering the similar BET values for L/T13c and LT/20c, the reason for the higher capacitance of L/T20c could be explained by the higher mesoporosity, at a range of 3−5 nm (Figure S3), which enhances the ion transport and the double layer adsorption of solvated ions.

When the scan rate increased from 10 to 100 mV s^{-1}, the specific capacitance decreased and L/T33c maintained 60% of the capacitance. In sum, the hierarchical porous structure of L/T33c enhances the ion transport in reaching the smaller pores at lower potential scan rates lead to a larger double layer capacitance.

Galvanostatic charge/discharge (GCD) measurements were carried out at different current densities, ranging from 0.6 to 6.3 mA cm^{-2} between 0 and 0.8 V. Figure 5c shows GCD profiles of the carbon microfibers at 0.6 mA cm^{-2}, illustrating approximately symmetrical charge and discharge behavior, which is characteristic of favorable electrochemical reversibility. In addition, a higher discharge time was observed for the carbon microfibers with higher TOCNF content (L/T33c > L/T20c > L/T13c > L/T5c). A small voltage drop in the discharge curve indicates energy losses due to the internal resistance and the mass transfer-limited mobility of the electrolyte ions in the microfiber pores. It is observed that the voltage drop decreases for carbon microfibers with higher TOCNF content (L/T33c < L/T20c < L/T13c < L/T5c), indicating less energy losses, i.e., enhanced charge transfer for T/L33c. The symmetrical GCD profiles of L/T33c at current

https://dx.doi.org/10.1021/acssuschemeng.0c00764
ACS Sustainable Chem. Eng. 2020, 8, 8549−8561

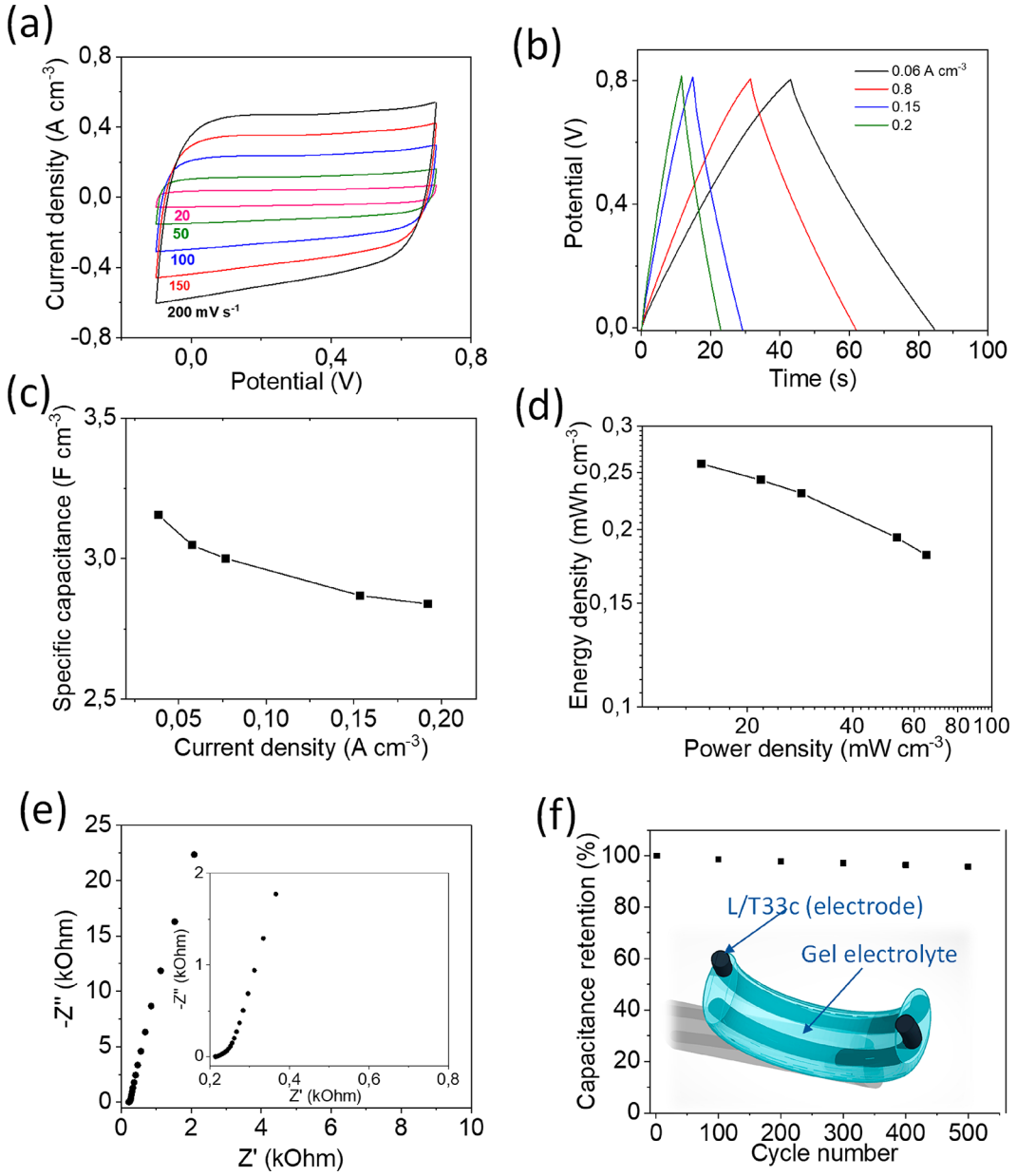

Figure 7. (a) CV curves of symmetrical FSC (made of two L/T33c carbon microfibers) at different scan rates. (b) GCD curves of symmetrical FSC and (c) specific capacitance at various current densities. (d) Ragone plot. (e) Nyquist plot recorded in the frequency range of 100 kHz to 0.01 Hz (inset: the high-frequency region of the plot). (f) Capacitance retention during stability cycles at 100 mV s^{-1}.

densities from 0.6 to 6.3 mA cm^{-2} (Figure 5d) also indicate that the double layer capacitance occurs reversibly in a wide range of current density.

To further understand the impedance characteristics of the carbon microfibers, EIS measurements were carried out over a frequency range of 0.01 Hz to 100 kHz. The Nyquist plots in Figure 5e mainly include a linear part in the low frequency region and a semicircle in the high frequency range, related to the polarization resistance (R_p). The small semicircle is likely induced by the redox features of quinone/hydroquinone groups in the carbon microfibers, as observed earlier in the CVs. In the low frequency region, the linear part (vertical lines to the real axis, Z′) reveal a capacitive behavior.[52] L/T33c shows the highest slope of such lines, followed by L/T20c, L/T13c, and finally L/T5c. The observations indicate an improved capacitive behavior with increasing TOCNF content. The high-frequency intersection of the plots at the real axis indicates the electrode series resistance (R_s). L/T5c and L/T33c show the lowest (108.5 ± 9 Ω) and highest (366.6 ± 51 Ω) value of R_s, respectively, while L/T13c and L/T20c displayed intermediate ranges. Bode plots in Figure 5f show the real values of impedance over the entire frequency range. The values at high frequency are related to the series resistance (R_s),[60] and a similar pattern in Nyquist plots can be observed. From the low frequency section, it can be inferred that the charge transfer resistance (R_p) is the lowest for L/T33c, thus validating better electrochemical behavior. It can be concluded that although the conductivity decreased with TOCNF loading in L/T33c, the capacitance was not significantly influenced by this variable (the conductivity was in a relatively narrow range of values, 42−62 S cm^{-1}). It was the surface area and porous

https://dx.doi.org/10.1021/acssuschemeng.0c00764
ACS Sustainable Chem. Eng. 2020, 8, 8549−8561

Table 3. Electrochemical Performance of the Reported FSC

materials	electrolyte	capacitance, F cm^{-3}	energy density, mWh cm^{-3}	power density, mW cm^{-3}	ref
CNT/RGO	PVA/H_2SO_4	68.4	2.4	16	63
RGO/CNT/PANI[a]	PVA/H_2SO_4	36.7	0.98	16.25	64
CNT/MnO_2 yarn	PVA/KOH	25.4	3.52	127	67
MnO_2/carbon fiber	PVA/H_3PO_4	2.5	0.22	8	68
RGO/CNT/PANI	PVA/H_3PO_4	0.18	3.5	18	65
MnO_2/CNT fiber	PVA/LiCl	10.9	1.5−0.96	50−2500	69
RGO/CNT	PVA/H_3PO_4	300	6.3	1085	66
MoS_2-rGO/CNT	PVA/H_2SO_4	5.2	1−3	∼90−1100	70
PEDOT/CNT	PVA/H_2SO_4	180	1.4	40000	71
PPY[b]/RGO/CNT	PVA/H_3PO_4	18.2	0.94	7.32	72
CNT/GF[c]	PVA/H_2SO_4	60.75	1.5−4.83	17.11−18.1	52
GRO/PANI	PVA/H_2SO_4	148	8.8	30.77	73
carbon microfiber	**PVA/H_2SO_4**	**2.8−3.1**	**0.25**	**65.1**	**this work**

[a]PANI: polyaniline; [b]PPY: polypyrrole. [c]GF: graphene fibers.

structure that were the main variables influencing the capacitance.

Next, the most promising carbon microfibers were further tested in terms of long-term cycling performance and electrode stability. As shown in Figure 6a, the microfiber electrodes exhibited excellent electrochemical stability after 5000 continuous cycles. L/T33c showed no loss of specific capacitance; on the contrary, a slight capacitance increase was observed. The increase in capacitance implies that there is gradual wetting and thus better access of electrolyte ions to the pores, especially relevant in stability tests that were carried out at slow scan rates (20 mV s^{-1}). Similar observations have been reported elsewhere.[59,61,62] The stability trends varied for the different samples, Figure 6a, likley due to the different pore distribution, as discussed earlier. To elucidate the effect of wetting, we soaked the carbon fibers in the electrolyte overnight, which were then subjected to longer stability tests, for up to 10,000 continuous cycles at 100 mV s^{-1}. As can be seen in Figure 6b, L/T33c retained its initial performance, by 93%, after 10,000 cycles. The CVs before and after stability tests (inset of Figure 6b) indicated minor performance loss after such long-term cycling. The XPS spectrum further proved that no chemical changes occurred on the surface of the carbon microfibers during H_2SO_4 (1 M) immersion in (Figure S7) or after stability evaluation (Figure S8).

Finally, a solid-state symmetric fiber supercapacitor (FSC) was fabricated using two L/T33c microfibers with PVA/H_2SO_4 gel electrolyte and covered with PDMS, forming a two-electrode cell configuration. Figure 7a shows the CV curves at different scan rates, indicating an ideal EDLC behavior, with rectangular profiles even at high scan rates (200 mV s^{-1}). The GCD curves at different current densities (Figure 7b) display excellent symmetry with minimal IR drop, suggesting good charge storage properties. The specific capacitance, around 3.1−2.8 F cm^{-3} (3.8−3.4 F g^{-1}), slightly decreased by increasing the current density, from 0.07 to 0.2 A g^{-1} (Figure 7c). A Ragone plot (Figure 7d) related the energy density and power density, with maximum values equal to 0.25 mWh cm^{-3} (0.33 Wh kg^{-1}), and power density of 65.1 mW cm^{-3} (84.7 Wh kg^{-1}). Table 3 includes the performance (energy and power density) of various FSCs. The energy and power density measured for the present system are on par with those reported for carbon nanotubes (CNTs) and graphene oxides (GO)[63−66] as well as metal oxide[67−70] and conductive polymers.[64,65,71,72] Nyquist plots from EIS measurements in Figure 7e indicate a small intrinsic resistance (inset of Figure 7e), and the vertical straight line in the low-frequency region is a signal of good capacitive performance. Moreover, all solid-state symmetric FSCs based on L/T33c exhibited excellent electrochemical stability, above 96% after 500 cycles (Figure 7f).

One final point related to the use of the carbon microfibers is that of their bendability, which is limited in the present case given the relatively large diameter of the microfibers. It can be expected that bendability (and overall mechanical strength) could be improved if fibers of smaller diameters were produced.

Overall, the introduced facile method for preparation of porous and conductive carbon microfibers represents an opportunity toward 1-D electrodes. They can be deployed as environmentally friendly, fiber-shaped energy-storage devices for small portable and wearable applications. Application in organic bioelectronics can be foreseen. In addition, coupling the synthesized, porous carbon microfibers with conductive polymers or metal-oxides in core−shell device configurations is expected to lead to gains in pseudocapacitance.

CONCLUSIONS

Carbon microfibers were obtained by wet spinning of aqueous suspensions of lignocellulose nanofibrils (LCNF) derived from mechanical wood fibers followed by carbonization at 900 °C. The addition of only 5% TOCNF in the spinning dope significantly enhanced the spinnability of LCNF. A further increase of TOCNF to 33%, improved the morphology and the mechanical properties of the obtained microfibers (increasing by 3 times the Young's modulus and tensile strength). The carbon yield and conductivity increased with LCNF loading, owing to the high lignin content. Meanwhile, the pore evolution after carbonization was mainly affected by TOCNF content in the spinning dope. The surface area and porosity were both increased with TOCNF loading (from 5 to 33%) and resulted in improved capacitance (from 2.4 to 25 F cm^{-3}). The carbon microfibers showed excellent long-term stability (93% retention after 10,000 cycles). All-solid state supercapacitor performed stably, with an energy density of 0.25 mWh cm^{-3} (0.33 Wh kg^{-1}) and power density of 65.1 mW cm^{-3} (84.7 Wh kg^{-1}), demonstrating a potential candidacy for integration in small portable and wearable electronics.

https://dx.doi.org/10.1021/acssuschemeng.0c00764
ACS Sustainable Chem. Eng. 2020, 8, 8549−8561

■ ASSOCIATED CONTENT

Supporting Information

The Supporting Information is available free of charge at https://pubs.acs.org/doi/10.1021/acssuschemeng.0c00764.

LCNF chemical composition (Table S1); SEM images of the cross-section of LCNF-based microfibers before carbonization (Figure S1); appearance of the microfibers before and after carbonization (Figure S2); pore volume and width of carbon microfibers (Figure S3); cross section images of carbon microfibers (Figure S4); Raman spectra of carbonized LCNF/TOCNF filaments (Figure S5); CV curves of (a) L/T33c, (b) L/T20c, (c) L/T13c, and (d) L/T5c at different scan rates from 5 to 100 mV s^{-1} (Figure S6); XPS wide scans and C 1s HiRes regions for L/T33c before and after immersing in 1 M H_2SO_4 for 1 week (Figure S7); XPS wide scans and C 1s HiRes regions for L/T33c before and after 10,000 cycle stability test (Figure S8) (PDF)

■ AUTHOR INFORMATION

Corresponding Authors

Maryam Borghei − *Department of Bioproducts and Biosystems, Aalto University, Espoo 02150, Finland*; Email: maryam.borghei@aalto.fi

Orlando J. Rojas − *Department of Bioproducts and Biosystems, Aalto University, Espoo 02150, Finland; Departments of Chemical and Biological Engineering, Chemistry and Wood Science, University of British Columbia, Vancouver, British Columbia, Canada V6T 1Z3*; orcid.org/0000-0003-4036-4020; Email: orlando.rojas@ubc.ca

Authors

Ling Wang − *Department of Bioproducts and Biosystems, Aalto University, Espoo 02150, Finland*

Amal Ishfaq − *Department of Bioproducts and Biosystems, Aalto University, Espoo 02150, Finland*

Panu Lahtinen − *VTT Technical Research Centre of Finland, Espoo 02044, Finland*

Mariko Ago − *School of Science and Engineering, Meisei University, Hino, Tokyo 191-8606, Japan*

Anastassios C. Papageorgiou − *Turku Bioscience Centre, University of Turku and Åbo Akademi University, Turku 20520, Finland*; orcid.org/0000-0002-7980-1120

Meri J. Lundahl − *Department of Bioproducts and Biosystems, Aalto University, Espoo 02150, Finland*; orcid.org/0000-0003-0979-0486

Leena -Sisko Johansson − *Department of Bioproducts and Biosystems, Aalto University, Espoo 02150, Finland*

Tanja Kallio − *Department of Chemistry and Materials Science, Aalto University, Espoo 02150, Finland*; orcid.org/0000-0001-6671-8582

Complete contact information is available at: https://pubs.acs.org/10.1021/acssuschemeng.0c00764

Author Contributions

The manuscript was written through contributions of all authors. All authors have given approval to the final version of the manuscript.

Notes

The authors declare no competing financial interest.

■ ACKNOWLEDGMENTS

This work was partially funded by Business Finland through the strategic opening Design Driven Value Chains in the World of Cellulose, the H2020-ERC-2017-Advanced Grant "BioELCell" (788489) and the Canada Excellence Research Chair program. We acknowledge the Academy of Finland's Centers of Excellence program (project 264677, HYBER). M.L. is grateful to KAUTE, the Finnish Science Foundation for Technology and Economics, for their financial support. A.C.P. thanks Biocenter Finland for infrastructure support. We are thankful to Prof. Tapani Vuorinen as well Sappi-Finland for supplying samples of mechanical pulp. We also acknowledge Joseph Campbell for doing the XPS measurement. Finally, we appreciate the discussions and suggestions of Dr. Michael Hummel (Aalto), Hannes Orelma (VTT), and Daisuke Sawada (Aalto). We also acknowledge the use of premises in Aalto Nanomicroscopy center (Otanano) in this study.

■ REFERENCES

(1) Holmes, M. Global Carbon Fibre Market Remains on Upward Trend. *Reinf. Plast.* **2014**, *58* (6), 38−45.

(2) Dumanlı, A. G.; Windle, A. H. Carbon Fibres from Cellulosic Precursors: A Review. *J. Mater. Sci.* **2012**, *47* (10), 4236−4250.

(3) Ansell, P. M.; Mwaikambo, Y. L. The Structure of Cotton and Other Plant Fibres. In *Handbook of Textile Fibre Structure*; Eichhorn, S. J., Hearle, J. W. S., Jaffe, M., Kikutani, T., Eds.; Woodhead Publishing Limited: Boston, MA, 2009; pp 63−77.

(4) Ganster, J.; Fink, H. P. The Structure of Man-Made Cellulosic Fibres Vol. 2: Natural, Regenerated, Inorganic and Specialist Fibres. In *Handbook of Textile Fibre Structure*; Eichhorn, S., Hearle, J. W. S., Jaffe, M., Kikutani, T., Eds.; Woodhead Publishing Limited: Boston, 2009; pp 201−233.

(5) Lundahl, M. J.; Klar, V.; Wang, L.; Ago, M.; Rojas, O. J. Spinning of Cellulose Nanofibrils into Filaments: A Review. *Ind. Eng. Chem. Res.* **2017**, *56* (1), 8−19.

(6) Kamada, A.; Mittal, N.; Söderberg, L. D.; Ingverud, T.; Ohm, W.; Roth, S. V.; Lundell, F.; Lendel, C. Flow-Assisted Assembly of Nanostructured Protein Microfibers. *Proc. Natl. Acad. Sci. U. S. A.* **2017**, *114* (6), 1232−1237.

(7) Hooshmand, S.; Aitomäki, Y.; Norberg, N.; Mathew, A. P.; Oksman, K. Dry-Spun Single-Filament Fibers Comprising Solely Cellulose Nanofibers from Bioresidue. *ACS Appl. Mater. Interfaces* **2015**, *7*, 13022.

(8) Vuoriluoto, M.; Orelma, H.; Lundahl, M.; Borghei, M.; Rojas, O. J. Filaments with Affinity Binding and Wet Strength Can Be Achieved by Spinning Bifunctional Cellulose Nanofibrils. *Biomacromolecules* **2017**, *18*, 1803−1813.

(9) Wang, L.; Lundahl, M. J.; Greca, L. G.; Papageorgiou, A. C.; Borghei, M.; Rojas, O. J. Effects of Non-Solvents and Electrolytes on the Formation and Properties of Cellulose I Filaments. *Sci. Rep.* **2019**, *9* (1), 1−11.

(10) Mittal, N.; Ansari, F.; Gowda.V, K.; Brouzet, C.; Chen, P.; Larsson, P. T.; Roth, S. V.; Lundell, F.; Wagberg, L.; Kotov, N. A.; Soderberg, L. D. Multiscale Control of Nanocellulose Assembly: Transferring Remarkable Nanoscale Fibril Mechanics to Macroscale Fibers. *ACS Nano* **2018**, *12* (7), 6378−6388.

(11) Bacon, R.; Tang, M. M. Carbonization of Cellulose Fibers—II. Physical Property Study. *Carbon* **1964**, *2* (3), 221−225.

(12) Byrne, N.; De Silva, R.; Ma, Y.; Sixta, H.; Hummel, M. Enhanced Stabilization of Cellulose-Lignin Hybrid Filaments for Carbon Fiber Production. *Cellulose* **2018**, *25* (1), 723−733.

(13) Ago, M.; Borghei, M.; Haataja, J. S.; Rojas, O. J. *RSC Adv.* **2016**, *6*, 85802−85810.

(14) Pratima, B. Raw Materials and Processes for the Production of Carbon Fibre. In *Update on Carbon Fibre*; iSmithers Rapra Publishing: Shropshire, 2013; pp 9−40, ISBN: 9781909030244.

(15) Baker, D. A.; Rials, T. G. Recent Advances in Low-Cost Carbon Fiber Manufacture from Lignin. *J. Appl. Polym. Sci.* **2013**, *130* (2), 713−728.
(16) Wang, L.; Ago, M.; Borghei, M.; Ishaq, A.; Papageorgiou, A.; Lundahl, M. J.; Rojas, O. J. Conductive Carbon Microfibers Derived from Wet-Spun Lignin/Nanocellulose Hydrogels. *ACS Sustainable Chem. Eng.* **2019**, *7*, 6013.
(17) Spence, K. L.; Venditti, R. A.; Rojas, O. J.; Habibi, Y.; Pawlak, J. J. A Comparative Study of Energy Consumption and Physical Properties of Microfibrillated Cellulose Produced by Different Processing Methods. *Cellulose* **2011**, *18* (4), 1097−1111.
(18) Chen, H.; Wang, X.; Bozell, J. J.; Feng, X.; Huang, J.; Li, Q.; Ragauskas, A. J.; Wang, S.; Mei, C. Effect of Solvent Fractionation Pretreatment on Energy Consumption of Cellulose Nanofabrication from Switchgrass. *J. Mater. Sci.* **2019**, *54* (10), 8010−8022.
(19) Wang, X.; Chen, H.; Feng, X.; Zhang, Q.; Labbé, N.; Kim, K.; Huang, J.; Ragauskas, A. J.; Wang, S.; Zhang, Y. Isolation and Characterization of Lignocellulosic Nanofibers from Four Kinds of Organosolv-Fractionated Lignocellulosic Materials. *Wood Sci. Technol.* **2020**, 1−15.
(20) Jan, S. History of Mechanical Pulping. In *Mechanical Pulping (Papermaking Science and Technology)*; Lönnberg, B., Ed.; Paper Engineers' Association/Paperi ja Puu Oy: Jyväskylä, 2009; pp 24−34, ISBN: 978−952−5216−35−6.
(21) Sundholm, J. Idea of Mechanical Pulping. In *Mechanical Pulping (Papermaking Science and Technology)*; Lönnberg, B., Ed.; Paper Engineers' Association/Paperi ja Puu Oy: Jyväskylä, 2009; pp 18−22, ISBN: 978−952−5216−00−4.
(22) Varhimo, A.; Sirviö, J.; Tuovinen, O. Wood Raw Materials. In *Mechanical Pulping (Papermaking Science and Technology)*; Lönnberg, B., Ed.; Paper Engineers' Association/Paperi ja Puu Oy: Jyväskylä, 2009; pp 70−109.
(23) Nguyen, N. A.; Kim, K.; Bowland, C. C.; Keum, J. K.; Kearney, L. T.; André, N.; Labbé, N.; Naskar, A. K. A Fundamental Understanding of Whole Biomass Dissolution in Ionic Liquid for Regeneration of Fiber by Solution-Spinning. *Green Chem.* **2019**, *21* (16), 4354−4367.
(24) Wang, Z.; Han, Y.; Zeng, Y.; Qie, Y.; Wang, Y.; Zheng, D.; Lu, X.; Tong, Y. Activated Carbon Fiber Paper with Exceptional Capacitive Performance as a Robust Electrode for Supercapacitors. *J. Mater. Chem. A* **2016**, *4* (16), 5828−5833.
(25) Zhao, X.; Lu, X.; Tze, W. T. Y.; Wang, P. A Single Carbon Fiber Microelectrode with Branching Carbon Nanotubes for Bioelectrochemical Processes. *Biosens. Bioelectron.* **2010**, *25*, 2343−2350.
(26) Gao, L.; Surjadi, J. U.; Cao, K.; Zhang, H.; Li, P.; Xu, S.; Jiang, C.; Song, J.; Sun, D.; Lu, Y. Flexible Fiber-Shaped Supercapacitor Based on Nickel−Cobalt Double Hydroxide and Pen Ink Electrodes on Metallized Carbon Fiber. *ACS Appl. Mater. Interfaces* **2017**, *9* (6), 5409−5418.
(27) Zhou, Z.; Zhang, Q.; Sun, J.; He, B.; Guo, J.; Li, Q.; Li, C.; Xie, L.; Yao, Y. Metal−Organic Framework Derived Spindle-like Carbon Incorporated α-Fe $_2$ O $_3$ Grown on Carbon Nanotube Fiber as Anodes for High-Performance Wearable Asymmetric Supercapacitors. *ACS Nano* **2018**, *12* (9), 9333−9341.
(28) Guo, J.; Zhang, Q.; Sun, J.; Li, C.; Zhao, J.; Zhou, Z.; He, B.; Wang, X.; Man, P.; Li, Q.; Zhang, J.; Xie, L.; Li, M.; Yao, Y. Direct Growth of Vanadium Nitride Nanosheets on Carbon Nanotube Fibers as Novel Negative Electrodes for High-Energy-Density Wearable Fiber-Shaped Asymmetric Supercapacitors. *J. Power Sources* **2018**, *382*, 122−127.
(29) Liao, M.; Ye, L.; Zhang, Y.; Chen, T.; Peng, H. The Recent Advance in Fiber-Shaped Energy Storage Devices. *Advanced Electronic Materials* **2019**, *5* (1), 1800456.
(30) Wu, J.; Hong, Y.; Wang, B. The Applications of Carbon Nanomaterials in Fiber-Shaped Energy Storage Devices. *J. Semicond.* **2018**, *39* (1), 011004.
(31) Shi, X.; Zheng, S.; Wu, Z.; Bao, X. Recent Advances of Graphene-Based Materials for High-Performance and New-Concept Supercapacitors. *J. Energy Chem.* **2018**, *27* (1), 25−42.
(32) Meng, F.; Li, Q.; Zheng, L. Flexible Fiber-Shaped Supercapacitors: Design, Fabrication, and Multi-Functionalities. *Energy Storage Materials* **2017**, *8*, 85−109.
(33) Zhao, J.; Zhang, Y.; Huang, Y.; Xie, J.; Zhao, X.; Li, C.; Qu, J.; Zhang, Q.; Sun, J.; He, B.; Li, Q.; Lu, C.; Xu, X.; Lu, W.; Li, L.; Yao, Y. 3D Printing Fiber Electrodes for an All-Fiber Integrated Electronic Device via Hybridization of an Asymmetric Supercapacitor and a Temperature Sensor. *Advanced Science* **2018**, *5* (11), 1801114.
(34) Sluiter, A.; Hames, B.; Ruiz, R.; Scarlata, C.; Sluiter, J.; Templeton, D.; Crocker, D. Determination of Structural Carbohydrates and Lignin in Biomass. *Laboratory Analytical Procedure* **2008**, *1617*, 1−16.
(35) Yoshiharu, N.; Shigenori, K.; Masahisa, W.; Takeshi, O. Cellulose Microcrystal Film of High Uniaxial Orientation. *Macromolecules* **1997**, *30* (20), 6395−6397.
(36) Orelma, H.; Tanaka, A.; Rautkoski, H.; Nurminen, I.; Kouko, J.; Koponen, A. Mechanically Ground Softwood Fines as a Raw Material for Cellulosic Applications. *Cellulose* **2017**, *24*, 3869.
(37) Kirk, T. K.; Yang, H. H. Partial Delignification of Unbleached Kraft Pulp with Ligninolytic Fungi. *Biotechnol. Lett.* **1979**, *1* (9), 347−352.
(38) Shoham, Y.; Schwartz, Z.; Khasin, A.; Gat, O.; Zosim, Z.; Rosenberg, E. Delignification of Wood Pulp by a Thermostable Xylanase from Bacillus Stearothermophilus Strain T-6. *Biodegradation* **1992**, *3* (2), 207−218.
(39) Blechschmidt, J.; Heinemann, S. Latency and Properties of Mechanical Pulp. In *Handbook of Pulp*; Wiley: Weinheim, Germany, 2006; 1137−1145, DOI: 10.1002/9783527619887.ch18.
(40) Yan, Y.; Herzele, S.; Mahendran, A. R.; Edler, M.; Griesser, T.; Saake, B.; Li, J.; Gindl-Altmutter, W. Microfibrillated Lignocellulose Enables the Suspension-Polymerisation of Unsaturated Polyester Resin for Novel Composite Applications. *Polymers* **2016**, *8* (7), 255.
(41) Torres-Rendon, J. G.; Schacher, F. H.; Ifuku, S.; Walther, A. Mechanical Performance of Macrofibers of Cellulose and Chitin Nanofibrils Aligned by Wet-Stretching: A Critical Comparison. *Biomacromolecules* **2014**, *15* (7), 2709−2717.
(42) Yao, J.; Chen, S.; Chen, Y.; Wang, B.; Pei, Q.; Wang, H. Macrofibers with High Mechanical Performance Based on Aligned Bacterial Cellulose Nanofibers. *ACS Appl. Mater. Interfaces* **2017**, *9* (24), 20330−20339.
(43) Håkansson, K. M. O.; Fall, A. B.; Lundell, F.; Yu, S.; Krywka, C.; Roth, S. V.; Santoro, G.; Kvick, M.; Prahl Wittberg, L.; Wågberg, L.; Söderberg, L. D. Hydrodynamic Alignment and Assembly of Nanofibrils Resulting in Strong Cellulose Filaments. *Nat. Commun.* **2014**, *5*, 4018 DOI: 10.1038/ncomms5018.
(44) Li, Y.; Zhu, H.; Shen, F.; Wan, J.; Han, X.; Dai, J.; Dai, H.; Hu, L. Highly Conductive Microfiber of Graphene Oxide Templated Carbonization of Nanofibrillated Cellulose. *Adv. Funct. Mater.* **2014**, *24* (46), 7366−7372.
(45) Hu, X.; Xiong, W.; Wang, W.; Qin, S.; Cheng, H.; Zeng, Y.; Wang, B.; Zhu, Z. Hierarchical Manganese Dioxide/Poly(3,4-Ethylenedioxythiophene) Core−Shell Nanoflakes on Ramie-Derived Carbon Fiber for High-Performance Flexible All-Solid-State Supercapacitor. *ACS Sustainable Chem. Eng.* **2016**, *4* (3), 1201−1211.
(46) Shah, K. J.; Imae, T. Photoinduced Enzymatic Conversion of CO2 Gas to Solar Fuel on Functional Cellulose Nanofiber Films. *J. Mater. Chem. A* **2017**, *5* (20), 9691−9701.
(47) Lin, B.-J.; Chen, W.-H. Sugarcane Bagasse Pyrolysis in a Carbon Dioxide Atmosphere with Conventional and Microwave-Assisted Heating. *Front. Energy Res.* **2015**, *3*, 1−9.
(48) Jradi, K.; Maury, C.; Daneault, C. Contribution of TEMPO-Oxidized Cellulose Gel in the Formation of Flower-Like Zinc Oxide Superstructures: Characterization of the TOCgel/ZnO Composite Films. *Appl. Sci.* **2015**, *5* (4), 1164−1183.
(49) Shao, Y.; Guizani, C.; Grosseau, P.; Chaussy, D.; Beneventi, D. Thermal Characterization and Kinetic Analysis of Microfibrillated

Cellulose/Lignosulfonate Blends. *J. Anal. Appl. Pyrolysis* **2017**, *124*, 25−34.
(50) Fukuzumi, H.; Saito, T.; Okita, Y.; Isogai, A. Thermal Stabilization of TEMPO-Oxidized Cellulose. *Polym. Degrad. Stab.* **2010**, *95* (9), 1502−1508.
(51) Chen, G.; Chen, T.; Hou, K.; Ma, W.; Tebyetekerwa, M.; Cheng, Y.; Weng, W.; Zhu, M. Robust, Hydrophilic Graphene/Cellulose Nanocrystal Fiber-Based Electrode with High Capacitive Performance and Conductivity. *Carbon* **2018**, *127*, 218−227.
(52) Park, H.; Ambade, R. B.; Noh, S. H.; Eom, W.; Koh, K. H.; Ambade, S. B.; Lee, W. J.; Kim, S. H.; Han, T. H. Porous Graphene-Carbon Nanotube Scaffolds for Fiber Supercapacitors. *ACS Appl. Mater. Interfaces* **2019**, *11* (9), 9011−9022.
(53) Borghei, M.; Azcune, I.; Carrasco, P. M.; Sainio, J.; Kauppinen, E.; Ruiz, V. Nitrogen-Doped Graphene with Enhanced Oxygen Reduction Activity Produced by Pyrolysis of Graphene Functionalized with Imidazole Derivatives. *Int. J. Hydrogen Energy* **2014**, *39* (24), 12749−12756.
(54) Li, Y.; Sheng, K.; Yuan, W.; Shi, G. A High-Performance Flexible Fibre-Shaped Electrochemical Capacitor Based on Electrochemically Reduced Graphene Oxide. *Chem. Commun.* **2013**, *49* (3), 291−293.
(55) Lee, H.; Lee, G.; Yun, J.; Keum, K.; Hong, S. Y.; Song, C.; Kim, J. W.; Lee, J. H.; Oh, S. Y.; Kim, D. S.; Kim, M. S.; Ha, J. S. Facile Fabrication of a Fully Biodegradable and Stretchable Serpentine-Shaped Wire Supercapacitor. *Chem. Eng. J.* **2019**, *366*, 62−71.
(56) Gui, Q.; Wu, L.; Li, Y.; Liu, J. Scalable Wire-Type Asymmetric Pseudocapacitor Achieving High Volumetric Energy/Power Densities and Ultralong Cycling Stability of 100 000 Times. *Advanced Science* **2019**, *6* (10), 1802067.
(57) Gao, L.; Fan, R.; Xiao, R.; Cao, K.; Li, P.; Wang, W.; Lu, Y. NiO-Bridged MnCo-Hydroxides for Flexible High-Performance Fiber-Shaped Energy Storage Device. *Appl. Surf. Sci.* **2019**, *475*, 1058−1064.
(58) Naderi, L.; Shahrokhian, S. Nickel Molybdate Nanorods Supported on Three-Dimensional, Porous Nickel Film Coated on Copper Wire as an Advanced Binder-Free Electrode for Flexible Wire-Type Asymmetric Micro-Supercapacitors with Enhanced Electrochemical Performances. *J. Colloid Interface Sci.* **2019**, *542*, 325−338.
(59) Serrapede, M.; Rafique, A.; Fontana, M.; Zine, A.; Rivolo, P.; Bianco, S.; Chetibi, L.; Tresso, E.; Lamberti, A. Fiber-Shaped Asymmetric Supercapacitor Exploiting RGO/Fe2O3 Aerogel and Electrodeposited MnOx Nanosheets on Carbon Fibers. *Carbon* **2019**, *144*, 91−100.
(60) Binitha, G.; Soumya, M. S.; Madhavan, A. A.; Praveen, P.; Balakrishnan, A.; Subramanian, K. R. V.; Reddy, M. V.; Nair, S. V.; Nair, A. S.; Sivakumar, N. Electrospun α-Fe2O3 Nanostructures for Supercapacitor Applications. *J. Mater. Chem. A* **2013**, *1* (38), 11698.
(61) Zhou, J.; Lian, J.; Hou, L.; Zhang, J.; Gou, H.; Xia, M.; Zhao, Y.; Strobel, T. A.; Tao, L.; Gao, F. Ultrahigh Volumetric Capacitance and Cyclic Stability of Fluorine and Nitrogen Co-Doped Carbon Microspheres. *Nat. Commun.* **2015**, *6* (1), 8503.
(62) He, N.; Shan, W.; Wang, J.; Pan, Q.; Qu, J.; Wang, G.; Gao, W. Mordant Inspired Wet-Spinning of Graphene Fibers for High Performance Flexible Supercapacitors. *J. Mater. Chem. A* **2019**, *7* (12), 6869−6876.
(63) Wang, B.; Fang, X.; Sun, H.; He, S.; Ren, J.; Zhang, Y.; Peng, H. Fabricating Continuous Supercapacitor Fibers with High Performances by Integrating All Building Materials and Steps into One Process. *Adv. Mater.* **2015**, *27* (47), 7854−7860.
(64) Liu, D.; Du, P.; Wei, W.; Wang, H.; Wang, Q.; Liu, P. Skeleton/Skin Structured (RGO/CNTs)@PANI Composite Fiber Electrodes with Excellent Mechanical and Electrochemical Performance for All-Solid-State Symmetric Supercapacitors. *J. Colloid Interface Sci.* **2018**, *513*, 295−303.
(65) Kou, L.; Huang, T.; Zheng, B.; Han, Y.; Zhao, X.; Gopalsamy, K.; Sun, H.; Gao, C. Coaxial Wet-Spun Yarn Supercapacitors for High-Energy Density and Safe Wearable Electronics. *Nat. Commun.* **2014**, *5* (1), 3754.
(66) Yu, D.; Goh, K.; Wang, H.; Wei, L.; Jiang, W.; Zhang, Q.; Dai, L.; Chen, Y. Scalable Synthesis of Hierarchically Structured Carbon Nanotube−Graphene Fibres for Capacitive Energy Storage. *Nat. Nanotechnol.* **2014**, *9* (7), 555−562.
(67) Choi, C.; Lee, J. A.; Choi, A. Y.; Kim, Y. T.; Lepró, X.; Lima, M. D.; Baughman, R. H.; Kim, S. J. Flexible Supercapacitor Made of Carbon Nanotube Yarn with Internal Pores. *Adv. Mater.* **2014**, *26* (13), 2059−2065.
(68) Xiao, X.; Li, T.; Yang, P.; Gao, Y.; Jin, H.; Ni, W.; Zhan, W.; Zhang, X.; Cao, Y.; Zhong, J.; Gong, L.; Yen, W.; Mai, W.; Chen, J.; Huo, K.; Chueh, Y.; Wang, Z.; Zhou, J. Fiber-Based All-Solid-State Flexible Supercapacitors for Self-Powered Systems. *ACS Nano* **2012**, *6* (10), 9200−9206.
(69) Shi, P.; Li, L.; Hua, L.; Qian, Q.; Wang, P.; Zhou, J.; Sun, G.; Huang, W. Design of Amorphous Manganese Oxide@Multiwalled Carbon Nanotube Fiber for Robust Solid-State Supercapacitor. *ACS Nano* **2017**, *11* (1), 444−452.
(70) Sun, G.; Zhang, X.; Lin, R.; Yang, J.; Zhang, H.; Chen, P. Hybrid Fibers Made of Molybdenum Disulfide, Reduced Graphene Oxide, and Multi-Walled Carbon Nanotubes for Solid-State, Flexible, Asymmetric Supercapacitors. *Angew. Chem., Int. Ed.* **2015**, *54* (15), 4651−4656.
(71) Lee, J. A.; Shin, M. K.; Kim, S. H.; Cho, H. U.; Spinks, G. M.; Wallace, G. G.; Lima, M. D.; Lepró, X.; Kozlov, M. E.; Baughman, R. H.; Kim, S. J. Ultrafast Charge and Discharge Biscrolled Yarn Supercapacitors for Textiles and Microdevices. *Nat. Commun.* **2013**, *4* (1), 1970.
(72) Wang, S.; Liu, N.; Su, J.; Li, L.; Long, F.; Zou, Z.; Jiang, X.; Gao, Y. Highly Stretchable and Self-Healable Supercapacitor with Reduced Graphene Oxide Based Fiber Springs. *ACS Nano* **2017**, *11* (2), 2066−2074.
(73) Li, P.; Jin, Z.; Peng, L.; Zhao, F.; Xiao, D.; Jin, Y.; Yu, G. Stretchable All-Gel-State Fiber-Shaped Supercapacitors Enabled by Macromolecularly Interconnected 3D Graphene/Nanostructured Conductive Polymer Hydrogels. *Adv. Mater.* **2018**, *30* (18), 1800124.

https://dx.doi.org/10.1021/acssuschemeng.0c00764
ACS Sustainable Chem. Eng. 2020, 8, 8549−8561